Effect of Cooling Rate on Microsegregation During Solidification of Superalloy INCONEL 718 Under Slow-Cooled Conditions

XIAO SHI, SHENG-CHAO DUAN, WEN-SHENG YANG, HAN-JIE GUO, and JING GUO

The solidification sequence, microstructural evolution, solid-liquid interface variation, interdendritic segregation, and elemental distribution of as-cast IN718 alloy at three slow-cooling rates (5, 10, and 20 °C/min) were investigated by differential scanning calorimetry (DSC), confocal laser scanning microscopy (CLSM), optical microscopy (OM), field-emission scanning electron microscopy (FESEM), and electron-probe microanalysis (EPMA) techniques. The results indicate that as the cooling rate decreases, the constitutional supercooling at the solidification front affects the solid-liquid interface more significantly, and the size and quantity of the Laves phase increase. However, the composition of the Laves phase is insensitive to the cooling rate in the range of conditions studied here. In dendrite core, the contents of Ni, Cr, Fe, and Al follow a slight downward trend with an increasing cooling rate, whereas the Nb, Mo, and Ti contents show an upward trend. Additionally, Mo shows a stronger propensity to segregate under slow-cooling conditions because its effective partition coefficient almost linearly decreased with decreasing cooling rate, which is same as Nb. Using the parameters experimentally determined in this study and the Clyne–Kurz equation, we achieved reasonable agreement between the calculated and measured liquid composition change during the solidification process at different cooling rates. All experimental and theoretical programs in this research were undertaken with the aim of gaining further understanding of the microsegregation behaviors in large-scale IN718 ingots, whose cooling rates are within a lower range.

I. INTRODUCTION

NICKEL-BASED superalloy INCONEL 718 (IN718) is extensively used as raw materials to manufacture components for aerospace, marine, nuclear, and power-generation industries because of its combination of good corrosion resistance, high rupture strength, good mechanical properties, outstanding weldability, and excellent high-temperature structural stability in the range from – 253 °C to 650 °C.[1–3] The strengthening mechanism is mainly contributed by nanoscale particles that precipitate from solid-solution matrix (γ phase) during heat treatment and aging processes. One type of the principal strengthening phases is face-centered cubic intermetallic γ'-Ni$_3$(Al,Ti), and the other is metastable intermetallic γ''-Ni$_3$Nb with a body-centered tetragonal crystal structure. Mo is frequently added to IN718 to increase the mechanical resistance through solid-solution hardening.[2,4,5] However, in the solidification process, before heat treatment or forging, if the actual cooling rate is larger than the equilibrium rate, which is extremely slow, the high content of strengthening elements such as Nb, Mo, Al, and Ti in the IN718 alloy will be redistributed at the solidification front to various degrees. Therefore, the solid phases that crystallize at each temperature interval have different chemical compositions and do not have sufficient time to diffuse evenly, leading to the formation of a non-uniform matrix and detrimental brittle intermetallic compounds. Inevitably, this solute redistribution during non-equilibrium solidification will not only cause severe element segregation but also greatly affect the microstructure and morphology, resulting in considerable difficulties in the subsequent thermal processing

XIAO SHI, SHENG-CHAO DUAN, WEN-SHENG YANG, HAN-JIE GUO, and JING GUO are with the School of Metallurgical and Ecological Engineering, University of Science and Technology Beijing, Beijing 100083, China and also with the Beijing Key Laboratory of Special Melting and Preparation of High-End Metal Materials, Beijing 100083, China. Contact e-mail: guohanjie@ustb.edu.cn

and in significant deterioration of the final casting properties.

On the basis of the aforementioned phenomenon, several experimental methods have been employed to investigate the solidification behaviors of IN718 super-alloy.[6–11] In general, the as-cast IN718 alloy exhibits $L\rightarrow(\gamma + NbC)$ and $L\rightarrow(\gamma + Laves)$ eutectic-type reactions during solidification. Two minor microstructural segregation constituents, NbC and Laves, are known to precipitate in the solute-rich interdendritic liquid at different stages of solidification. Fe and Si additions increase the amount of the γ/Laves constituent, whereas C additions promote the formation of γ/NbC. Furthermore, various segregative mechanisms and experimental techniques have been developed to explain the elemental partitioning and change in liquid density during solidification.[12–18] These studies confirms that Nb, Si, and C exhibit a strong propensity to form secondary phases and that the depletion of Nb from dendrites primarily promotes the formation of interdendritic precipitates. In addition, the propensity of the remaining liquid density to increase with decreasing temperature will reverse because of the generation of the Laves phase, resulting in system instability. Moreover, literature on the solidification of IN718 alloy over a wide range of cooling rates has shown that a large cooling rate can inhibit the formation of the Laves phase, but the number of lattice defects will also increase.[19,20] These findings provide a variety of valuable solidification information and can be used to predict or control microsegregation during casting or welding. With the development of aviation and land-based turbine disk industries, greater demands will be placed on larger-sized IN718 castings and ingots. The larger size gives rise to an unavoidable slower cooling rate in the inner section of ingots, which will dramatically increase the inhomogeneity of the chemical composition[16]; thus, differences in solidification characteristics under slow-cooled conditions may exist. Therefore, further work is required to reveal the elemental segregation and microstructural evolution in large-scale ingots, which is one of the most important limiting factors in large-sized nickel-based superalloy manufacturing.

Given the above introduction, the aim of this work is to investigate the microsegregation behaviors of IN718 alloy under slow-cooling conditions and to determine if new information can be found to describe the correlation between the cooling rate and solidification segregation. Furthermore, an *in situ* observation technique, confocal laser scanning microscopy (CLSM), was performed and combined with other detection methods, including differential scanning calorimetry (DSC), field-emission scanning electron microscopy (FESEM) and electron-probe microanalysis (EPMA), to comprehensively evaluate the evolution of the microstructure and morphology during solidification process.

II. EXPERIMENTAL PROCEDURES

In contrast to experimental-scale IN718 ingots, commercial-scale ingots are too costly to study.

Nevertheless, studies have found that the temperature gradient (G) and solidification rate (R) are the most fundamental solidification parameters determining the microstructure and morphology.[13,21] A relatively constant G/R ratio corresponds to a common crystal morphology (measurement of constitutional supercooling), and the value of GR represents an invariant scale of microstructure (characterization of the cooling rate). According to this, an experimental-scale IN718 ingot was used to conduct fundamental research. If the variation of microstructure and microsegregation at different typical industrial cooling rates are described and analyzed clearly in the laboratory, the characteristics that have been investigated could correspond to industrial samples, revealing common features and providing reference data. Given that the general range of the cooling rate in an industrial ingot is basically less than 20 °C/min,[22] three different cooling rates (5, 10, and 20 °C/min) for solidification experiments were designed. Much lower cooling rates were not investigated in these experiments because of the extended time costs and equipment limitations.

A. *Experimental Material and Compositions*

According to the IN718 superalloy standard ingredients (AMS 5596A),[19] a 21-kg ingot with a top diameter of 60 mm, tail diameter of 120 mm, and height of 260 mm was produced in a vacuum-induction melting (VIM) furnace. The AMS specification for IN718 and the analyzed chemical composition of the ingot are presented in Table I.

B. *DSC Measurements*

DSC experiments were conducted to identify the phase transformation temperatures during heating or cooling, depending on whether the reaction is endothermic or exothermic. An STA-449C-Jupiter model

Table I. Chemical Analysis of the Experimental IN718 Ingot Produced in VIM (Wt Pct)

Chemical Element	AMS 5596A Standard Range[19]	Measured Results
Ni	50.0 to 55.0	52.72
Cr	17.0 to 21.0	18.26
Nb	4.75 to 5.50	4.92
Mo	2.80 to 3.30	3.13
Al	0.20 to 0.80	0.43
Ti	0.65 to 1.15	1.13
C	0.08*	0.02
Si	0.35*	0.20
Mn	0.35*	0.09
P	0.015*	0.01
S	0.015*	0.01
N	NM**	0.003
O	NM**	0.0023
H	NM**	0.0004
Fe	balance	

*Maximum content.
**Not mentioned.

(NETZSCH Inc., Germany) simultaneous thermal analyzer was used to simulate non-equilibrium solidification. Non-isothermal DSC measurements were performed with two samples of 5 mm in diameter and 2 mm in height, which were taken from the center of the ingot. For DSC measurements, the steel samples were heated from room temperature to 1400 °C at a constant rate of 20 or 5 °C/min and then held for 3 minutes at 1400 °C to homogenize the chemical composition before being lowered at the same rate to 1000 °C. Phase transformation temperatures were taken as deviations from the baseline. Purified argon gas (≥99.999 pct) was used as a protective atmosphere in the chamber to prevent the samples from oxidizing during the DSC measurements.

C. In situ Observations

To directly observe the solidification processes of IN718 under different cooling rates and to obtain more beneficial information, an in situ observation method was carried out using CLSM. CSLM offers the advantageous real-time and continuous observation of the melting or crystallization process on the free surface at high temperatures. Specimens were taken from the center of the experimental ingot and machined into a disk (7.6 mm in diameter and 2.5 mm in height). Before the in situ observation, the samples were mirror polished and separately placed into high-purity alumina crucibles, which were in turn inserted into the chamber of the confocal laser scanning microscope (VL2000DX-SVF17SP, LASERTEC Inc., Japan). After the gases were evacuated from the chamber using a vacuum pump several times, the sample chamber was purged with ultra-pure argon gas to avoid oxidation of the sample surface.

In the first part of this experiment, three total solidification processes were performed. The samples were heated from room temperature to 1450 °C and held for 3 minutes to be melted evenly. The liquid sample was subsequently cooled to 1100 °C at a rate of 5, 10, or 20 °C/min. Finally, the furnace was powered off at 1100 °C to allow the sample to cool to room temperature (the cooling rate was approximately 300 °C/min at this stage). Real-time videos and pictures were simultaneously recorded during the entire process. It is believed that the solidification of a sample has commenced below the surface of the opaque melt and is gradually being revealed on the melt surface[23] because the thermocouple is in contact with the bottom of the alumina crucible. Thus, the temperature difference between the sample surface and bottom of the crucible is treated as a systematic error.[24]

To further investigate the features of the microsegregation and verify the modeling results, a continuous quenching experiment was designed. When the CLSM samples cooled from 1450 °C at a rate of 5 °C/min, the solidification process was interrupted at selected temperatures by quenching with helium gas. The quenching temperatures were as follows: 1320 °C, 1310 °C, 1300 °C, 1270 °C, 1250 °C, 1190 °C, and 1170 °C.

D. Microsegregation and Microstructure Studies

The samples observed in situ via CLSM were ground and mechanically polished for electron-probe microanalysis (EPMA) detection. An EPMA-1720H (SHIMADZU Inc., Japan), in backscattered electron mode, was used to determine the elements qualitatively and quantitatively in different areas. The K_α lines were used for elements such as Fe, Ni, Cr, Al, Ti, and C, whereas the L_α lines were used for Mo and Nb. Considering the EPMA voltage and the average atomic number, atomic weight, and density of the overlay deposit,[25] the electron-probe scanning step was set larger than 1 μm.

After the distribution analysis of the alloying elements, the samples were electrolytically etched in a solution of CrO_3 (15 g) + H_2SO_4 (10 mL) + H_3PO_4 (150 mL) at a voltage of 10 V for 10 s to reveal the dendritic structure. The microstructure was analyzed by OM and FESEM (SUPRA 55, ZEISS Inc., Germany). The secondary dendrite arm spacing (SDAS) and the volume fraction of the segregated phase were measured and calculated on the basis of the micrographs.

III. RESULTS AND DISCUSSION

A. Phase Transformation Temperatures

1. DSC measurements
The temperatures of the phase transformations in superalloys are closely related to their alloy content. However, the standard composition range of IN718 alloy is broad for some important elements; thus, discrepant compositions influence the precipitation behaviors of the secondary phases. Accordingly, the main purpose of the DSC measurements was to identify the reaction temperatures of the studied IN718 alloy and to set the temperature parameters for subsequent CLSM observation. Moreover, the influence trends of different cooling rates during solidification would also be revealed. Previous investigations[7,8,11,19] on the melting and solidification of IN718 alloys, as exemplified in Table II, provide some information about reaction temperatures; however, because of the various compositions and test conditions, they are inappropriate for this study.

Figure 1 shows the DSC curves of the experimental IN718 specimens at different heating or cooling rates. "$T_{ei,m}$" is extrapolated initial melting temperature, indicating a phase that just begins to melt during the heating process. "$T_{ef,m}$" is extrapolated end melting temperature, representing the end of a phase melting. "$T_{p,m}$" is the temperature of the endothermic peak. Similarly, "$T_{ei,c}$," "$T_{ef,c}$," and "$T_{p,c}$" are the temperatures of extrapolated initial cooling, extrapolated end cooling, and exothermic peak, respectively. The superscripts denote the reaction phase in each temperature range.

The two heating curves are equivalent in the DSC thermograms, showing two deviations from the baseline. When the sample is heated above 1172 °C, an endothermic peak is observed, showing the γ/Laves liquation

Table II. Results from Different Investigators for the Phase Transformation Temperatures in IN718 (°C)

Author	Knorovsky[7]	Cao[8]	Dahotre[11]	Antonsson[19]	DSC Results in this Study (20 °C/min)	DSC Results in this Study (5 °C/min)
Liquidus on heating	1362	1345	1351	1340	1346	1346
Liquidus on cooling	—	1315	1319	1337	1328	1324
Solidus on heating	—	—	—	1250	1172	1172
Solidus on cooling	—	—	—	1075	1163	1171
γ/NbC on heating	1258	1267	1259	—	1255	1250
γ/NbC on cooling	—	1262	1249	1280	—	1252
γ/laves on heating	—	1167	1180	—	1196	1196
γ/laves on cooling	1198	1162	1160	1160	1177	1179
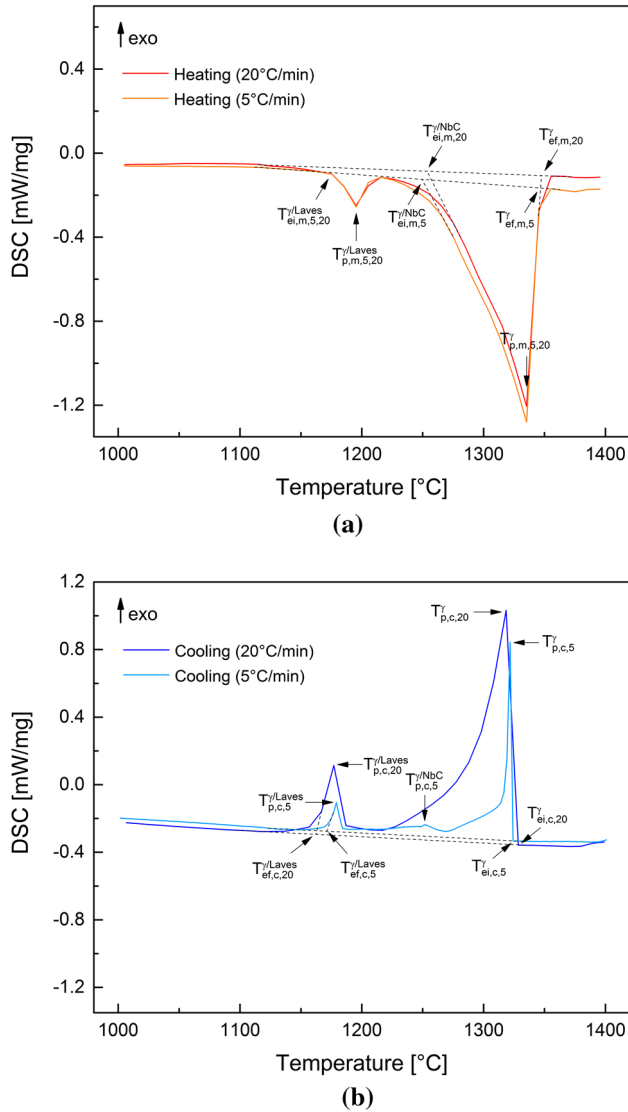
Fig. 1—DSC curves of experimental IN718 specimens: (*a*) heating; (*b*) cooling.

reaction emergence; thus, the solidus on heating is confirmed. Another larger endothermic peak lies between 1250 °C and 1335 °C, indicating melting of the bulk γ matrix accompanied by dissolution of NbC.

This wide temperature region may be due to the inhomogeneous γ dendrites, whose extremities melt first because of the enrichment of low-melting-point elements. With continued heating to 1346 °C, the samples melt completely and the DSC curves return to the baseline; thus, the liquidus on heating is confirmed. The current findings show that the different heating rates, within limits, do not affect the phase transformation temperatures.

During the cooling process, two solidification reactions can be observed, such as with the 20 °C/min curve. When the temperature decreases to approximately 1328 °C, the initial γ solid solutions first nucleate and grow in the liquid phase, releasing a large amount of latent heat of crystallization, resulting in a sharp exothermic peak. Subsequently, the reaction $L\rightarrow\gamma +$ NbC occurs, which depletes Nb and C in the residual liquid. Therefore, the composition of the local solidifying front reverts to the γ phase composition, with the slope of the DSC curve consequently becoming gradual until 1216 °C. The other distinct exothermic peak appears as the temperature decreases to approximately 1177 °C, at which the eutectic reaction $L\rightarrow\gamma +$ Laves is reached. The exothermic peak temperatures of these two reactions are relatively the same as the portion of the 5 °C/min cooling profile. More significantly, a subtle exothermic peak is observed at 1252 °C in the latter, indicating that the amount of NbC formed increases as a result of greater enrichment of the forming elements in the remaining liquid compared with the 20 °C/min curve. In addition, the average composition of the solid in the non-equilibrium solidification crystallized at each temperature interval is always lower than the equilibrium solidification because of the inhomogeneity of solute diffusion. Therefore, the practical solidus temperature is invariably lower than the equilibrium solidus temperature, and the higher the cooling rate, the greater the degree of this deviation.

2. CLSM observation

Figure 2 illustrates the CLSM *in situ* micrographs of nucleation and growth of the γ phase in the liquid steel during solidification at cooling rate of 5 °C/min. The γ solid phase first appears on the liquid surface when critical supercooling occurs at approximately 1325 °C. Along with continuous cooling to 1295 °C, many nuclei
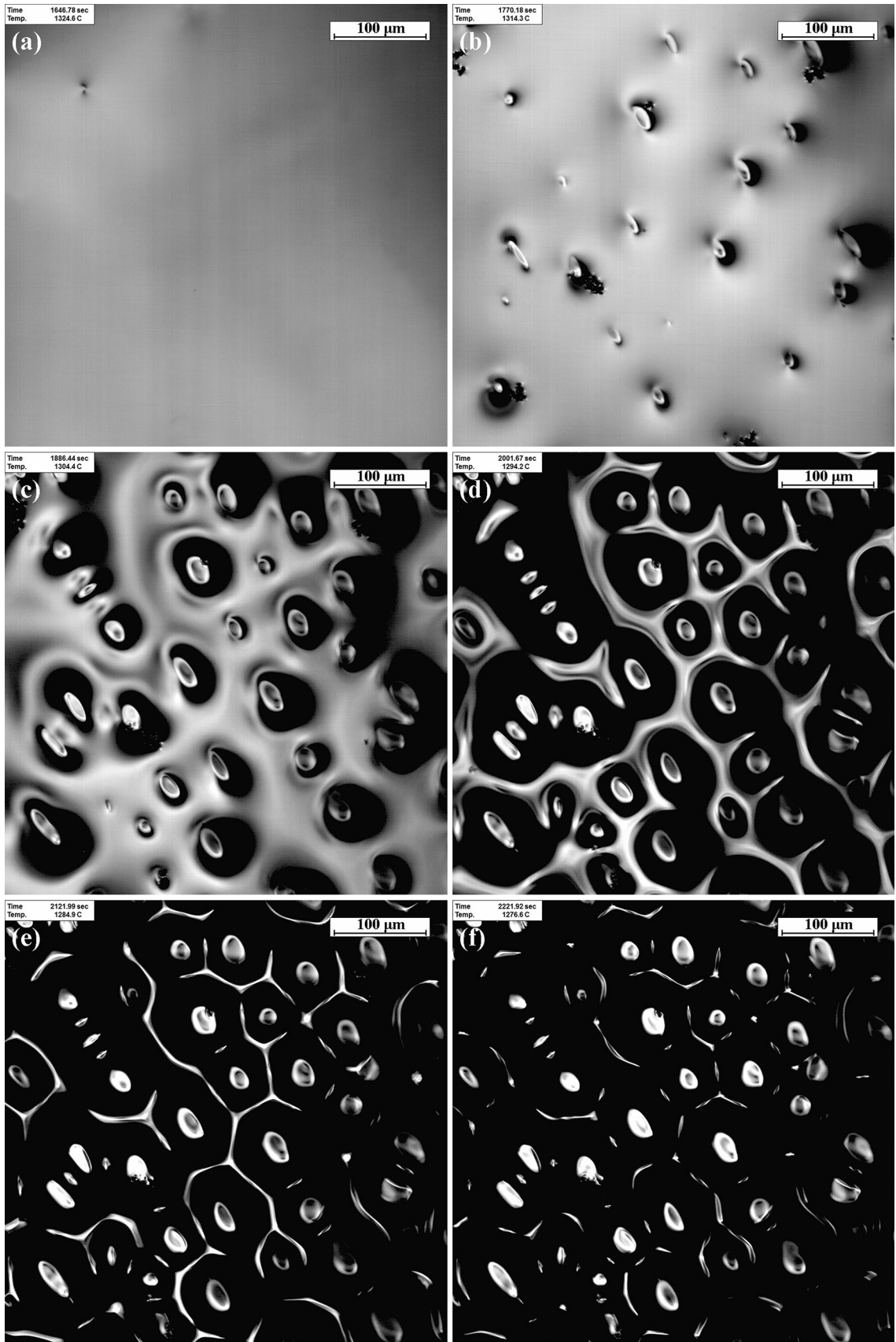
Fig. 2—*In situ* observation of the solidification process (5 °C/min) at different temperatures: (*a*) 1324.6 °C; (*b*) 1314.3 °C; (*c*) 1304.4 °C; (*d*) 1294.2 °C; (*e*) 1284.9 °C; (*f*) 1276.6 °C.

generate and quickly grow to form a cellular interface. With the further decrease of temperature, the liquid area continually decreases and forms a certain number of continuous reticular intercellular regions; simultaneously, the cellular structures grow into hexagonal-cell crystals. Coincidentally, these variations are the typical characteristics that a serious constitutional supercooling effects on the solidification front. Therefore, it is inferred that the residual liquid areas have a lower melting point than the solid portion because a large number of solutes were discharged from the solidifying front to the liquid during the solidification process. As a result, the most severe elemental segregation occurred in the intercellular groove position. Unfortunately, the undulating cellular morphology adversely affects the depth of field, which exceeds the equipment capability. Therefore, the morphological changes cannot be observed clearly below 1250 °C, especially those involved in the formation of γ/NbC and γ/Laves eutectic structures in interdendritic regions.

The tendency of the solid–liquid transition at various cooling rates in this study is similar to that observed at 5 °C/min; however, the arrangement and morphology of γ cells and liquid areas differ. Figure 3 shows typical micrographs of the γ phase forming at the intermediate stage of solidification during cooling at 10 and 20 °C/min. With an increasing cooling rate, the γ cell crystals become smaller and more irregular, and the intercellular regions change from continuous to discontinuous, portending that the constitutional supercooling has gradually weakened. Therefore, the lower the cooling rate, the more obvious the constitutional supercooling affects. This noticeable evidence also confirms that the constitutional supercooling strongly influences the

solid-liquid interface, which could affect the microstructures and properties of IN718 alloy.

B. Microstructural Characterizations

Figure 4 presents backscattered electron (BSE) images of the samples after CLSM observation. The notable difference between the γ phase and segregated phase confirms the occurrence of the inevitable solute segregation during non-equilibrium solidification. The γ dendrites that formed at higher cooling rates are finer and neater than those that formed at lower cooling rates. The morphology of the segregated phase changes from large-sized Chinese-character-like to small-sized block-like with increasing cooling rate. Moreover, the average volume fractions of the segregated phase in different samples were evaluated through multiple images using the Image-Pro Plus software (Figure 5), which revealed the segregated phase fraction, which also increases with decreasing cooling rate.

The EPMA results suggest that most of the segregated phase is Laves and that the remainder is MC (M = Nb and Ti). Figure 6 illustrates the average composition in the center of the Laves phase in samples cooled at different rates, as obtained from a large set of EPMA data, indicating that the composition of the Laves phase does not significantly change within a certain cooling rate range.

The microstructure and morphology of the Laves and MC were further investigated by FESEM on electrolytically etched specimens. Figures 7 and 8 show images of the segregated phase. The Laves is precipitated as distinct "islands" in the interdendritic regions, basically independent of the MC precipitation. With increasing
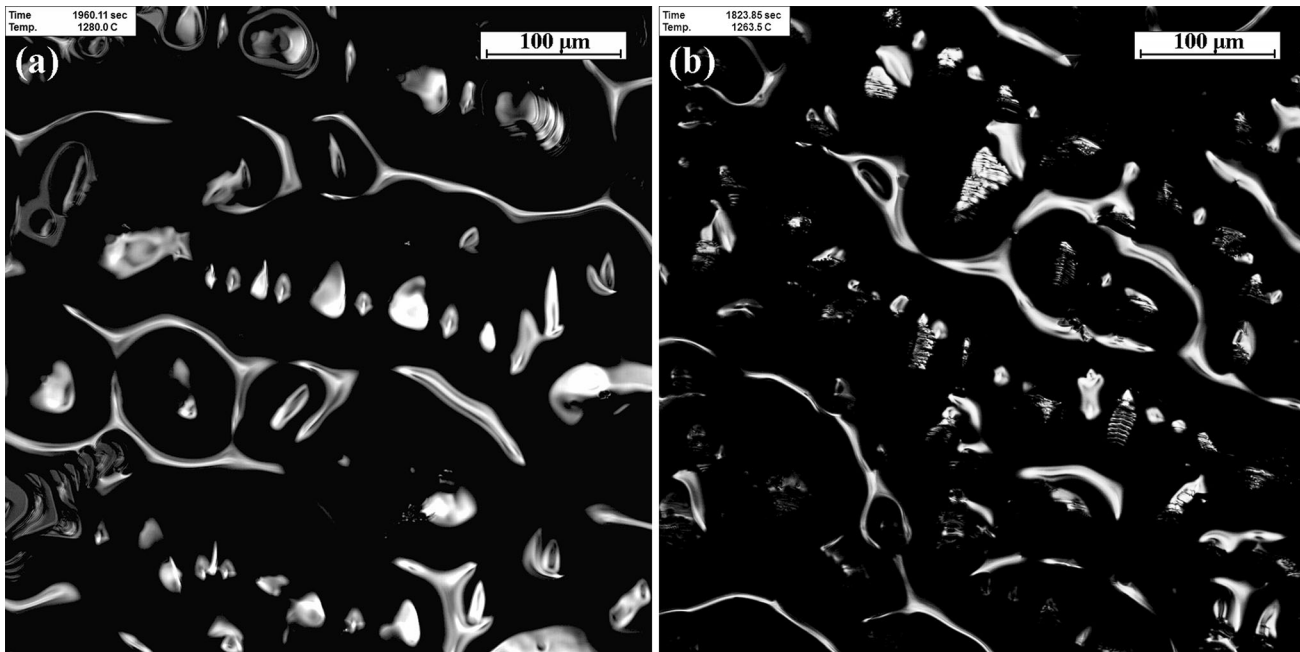

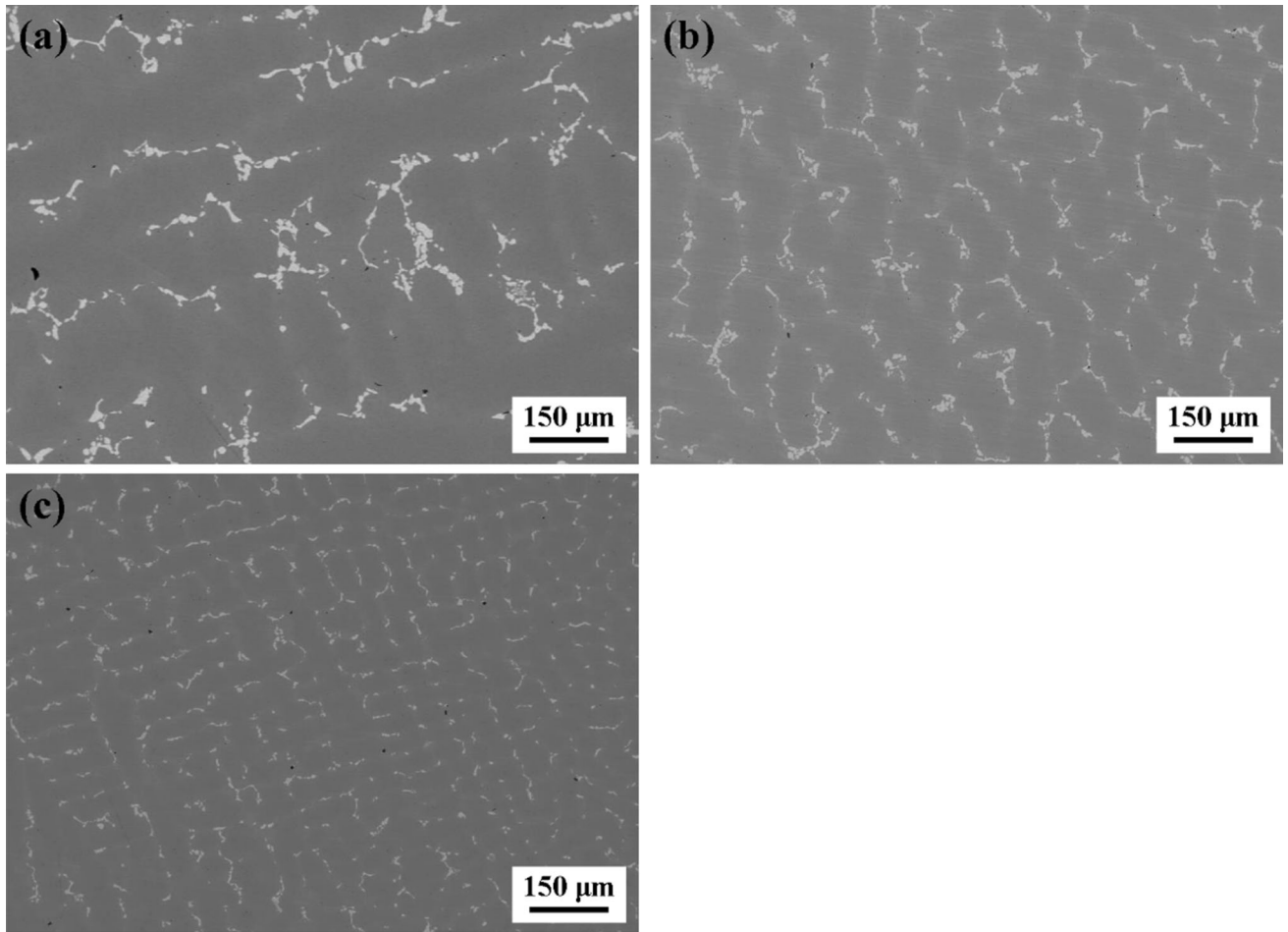Fig. 3—*In situ* observation of solidification process at various cooling rates: (*a*) 10 °C/min; (*b*) 20 °C/min.

Fig. 4—BSE images of samples under three cooling rates: (*a*) 5 °C/min; (*b*) 10 °C/min; (*c*) 20 °C/min.
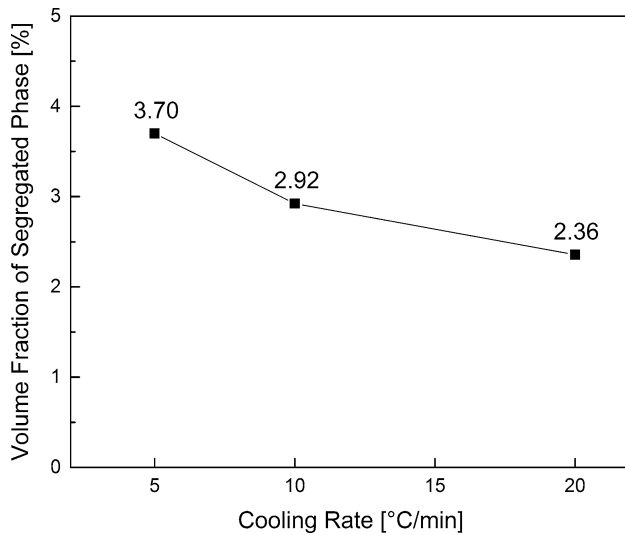

Fig. 5—Average volume fractions of the segregated phase in different cooling rate samples.

Fig. 6—Average chemical compositions of the Laves phase in samples cooled at different rates.

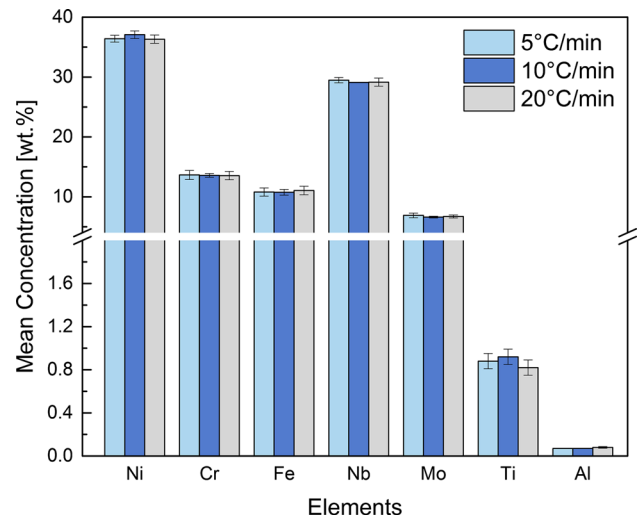cooling rate, the Laves phase becomes more dispersed, with a smaller particle size. In addition, a region is always observed around the Laves phase; this region is observed more clearly under the InLens signal (Figure 8). The EDS results indicate that the region is still γ phase, which has higher content of Nb, Ni, and Ti.
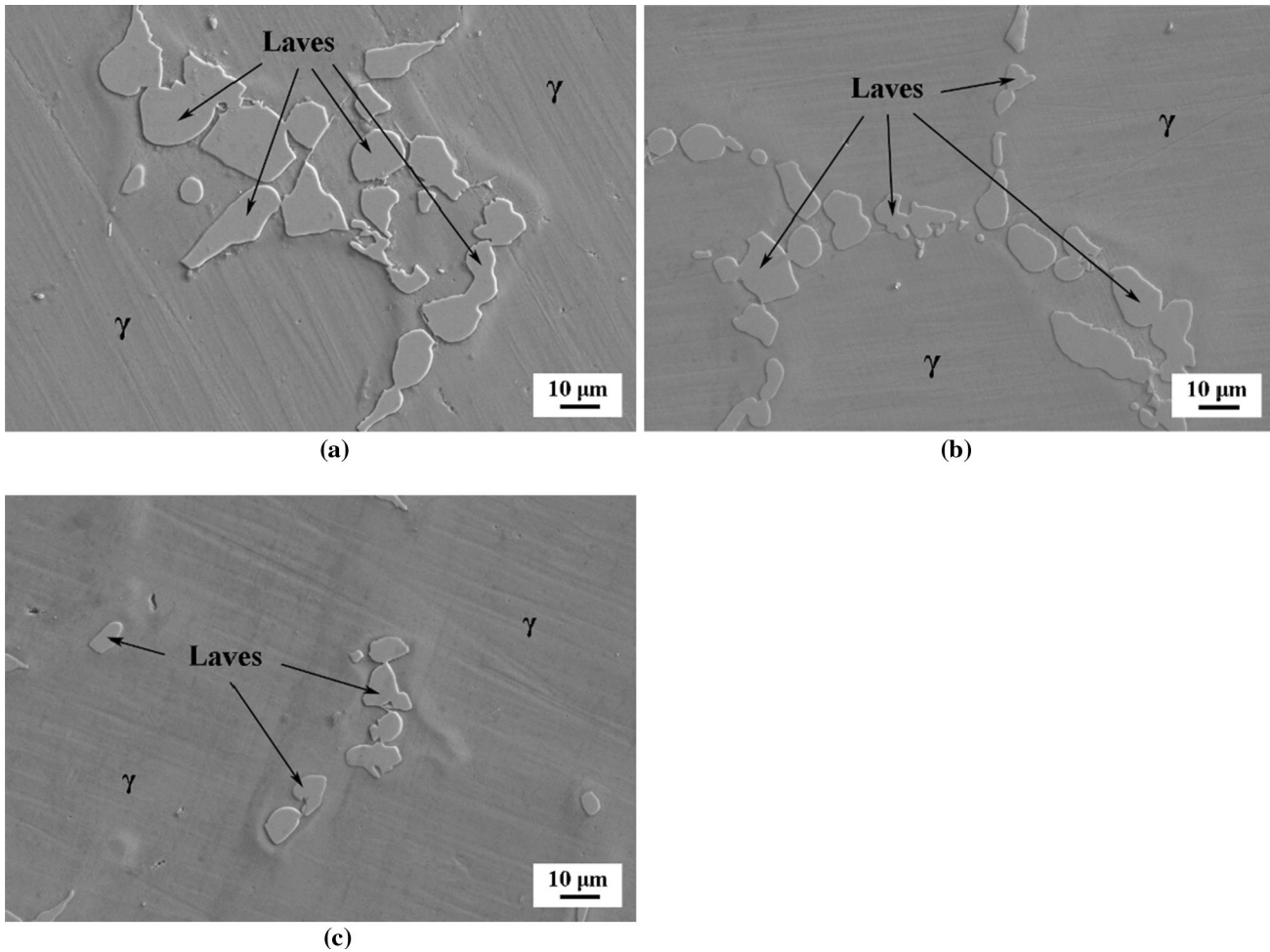
Fig. 7—FESEM images (SE2 signal) of the Laves phase on electrolytically etched samples at three cooling rates: (*a*) 5 °C/min; (*b*) 10 °C/min; (*c*) 20 °C/min.

This kind of phase can be taken as eutectic γ phase that forms together with Laves in the residual liquid at the terminal stage of solidification. Notably, no such phase is observed around the MC, which results from a divorced eutectic reaction.[19]

The average SDAS was measured in each sample (Table III), revealing that the SDAS decreases with increasing cooling rate.

The dendrite arm spacing is known to vary as a function of the temperature gradient (*G*, °C/mm) and the solidification growth rate (*R*, mm/min). For the SDAS (λ_2, μm), most of the theoretical treatments give the following functional form[21,26]:

$$\lambda_2 = b \times (GR)^{-1/3}, \qquad [1]$$

where *b* is a constant of the alloy. A linear relationship exists between λ_2 and $(GR)^{-1/3}$; thus, the slope of the line is *b*. The slope was calculated to be approximately 258 μm (°C/min)$^{1/3}$ based on linear regression shown in Figure 9. Thus, the prediction formula of SDAS in the cooling rate range studied here for IN718 is established:

$$\lambda_2 = 258 \times (GR)^{-1/3}. \qquad [2]$$

C. Element Segregation

It is confirmed that the solute redistribution occurs during non-equilibrium solidification, leading to element segregation. The composition profiles across a primary γ dendrite of each sample, after CLSM observation, were measured through EPMA to reveal the element distribution in dendrites. All the samples under different slow-cooling rates show the same trends in concentration patterns but differ in quantity.

Figure 10 shows the concentration profiles across a coarse dendrite of a sample cooled at 20 °C/min, as determined from EPMA line scans. Ni, Cr, and Fe are negative segregation elements with synchronous changes in dendrite and interdendritic areas. The contents of Fe and Cr decrease from the center to the periphery throughout the dendrite arm, whereas Ni shows enrichment to some extent in the dendrite edges and regions
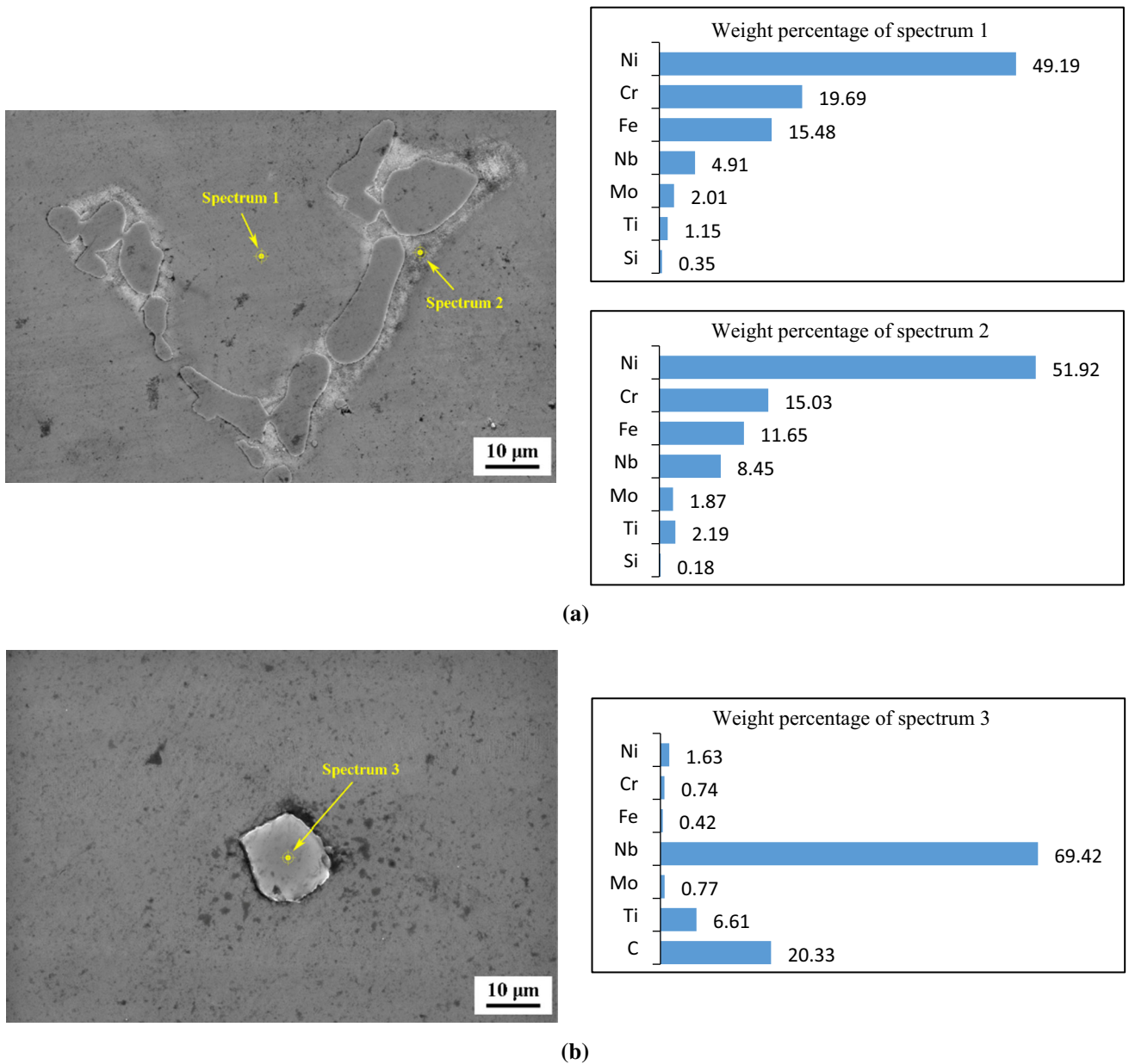
Fig. 8—FESEM images (InLens signal) and EDS analysis of an electrolytically etched sample cooled at 10 °C/min: (*a*) Laves; (*b*) MC.

Table III. Mean Values of SDAS Measured in Samples Cooled at Different Rates

Cooling Rate	5 °C/min	10 °C/min	20 °C/min
Mean SDAS (μm)	96 ± 3.6	67 ± 1.7	40 ± 2.6

between the adjacent Laves phase, where Ti is segregated at the same time. Additionally, Nb exhibits the strongest propensity to segregate in the Laves and MC phases and has a substantial minimum content in the central part of the dendrite. Ti is plentifully enriched in the MC, and it also has a minimum content in the dendrite core, which is a prominent effect of back diffusion. Mo is enriched only in the Laves phase, and the content of Mo changes little across the dendrite, possibly because of its lower diffusivity.

The content change of Ni, Cr, Fe, Al, and Ti in dendrite core under different cooling rates was evaluated by taking the average values of 20 points that were quantitatively measured by EPMA in the central part of dendrite arms. The concentrations of Ni, Cr, Fe, and Al tend to slightly decrease with a slow increase of cooling rate; Ti shows the opposite trend (Figure 11).

Table IV and Figure 12 illustrate the content change of Nb and Mo in dendrite core obtained by the same method, indicating that the Nb and Mo contents in the
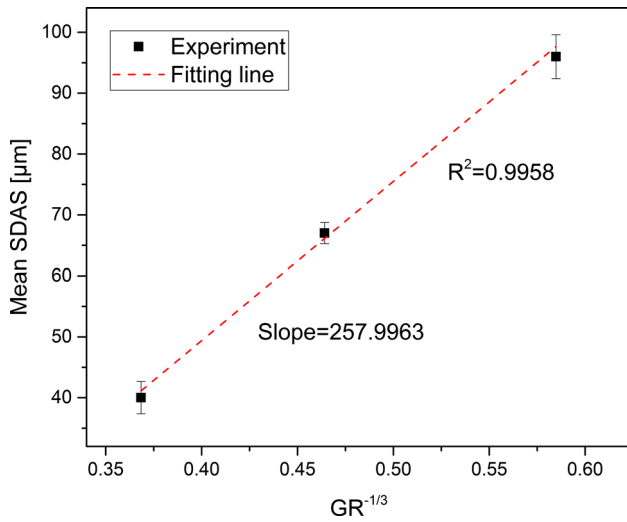
Fig. 9—The linear relation between the mean SDAS and $(GR)^{-1/3}$.

central part of the dendrite increase with increasing cooling rate. Therefore, the solubility in the primary γ phase of Nb and Mo increased with an increasing cooling rate. Moreover, if the content is replaced by the effective partition coefficient (k_e), which is calculated by dividing the measured average data by the nominal composition analysis reported in Table I, a significant linear relationship is observed between the k_e and the cooling rate, as also shown in Figure 12. This result is similar to that reported in Reference 19 where the authors analyzed the variation of k_e[Nb] over a wide range of cooling rates. The value of k_e provides an extent of the segregation effects—specifically, a solute with lower k_e segregates more strongly to the liquid phase during solidification process.[25] This phenomenon predicts that an increase in cooling rate gives rise to a reduction of the solute enrichment level at the solidification front.

Moreover, the k_e[Mo] will tend to a value of 1 earlier than k_e[Nb] when the cooling rate is increased further; therefore, the segregation degree of Mo can be ignored
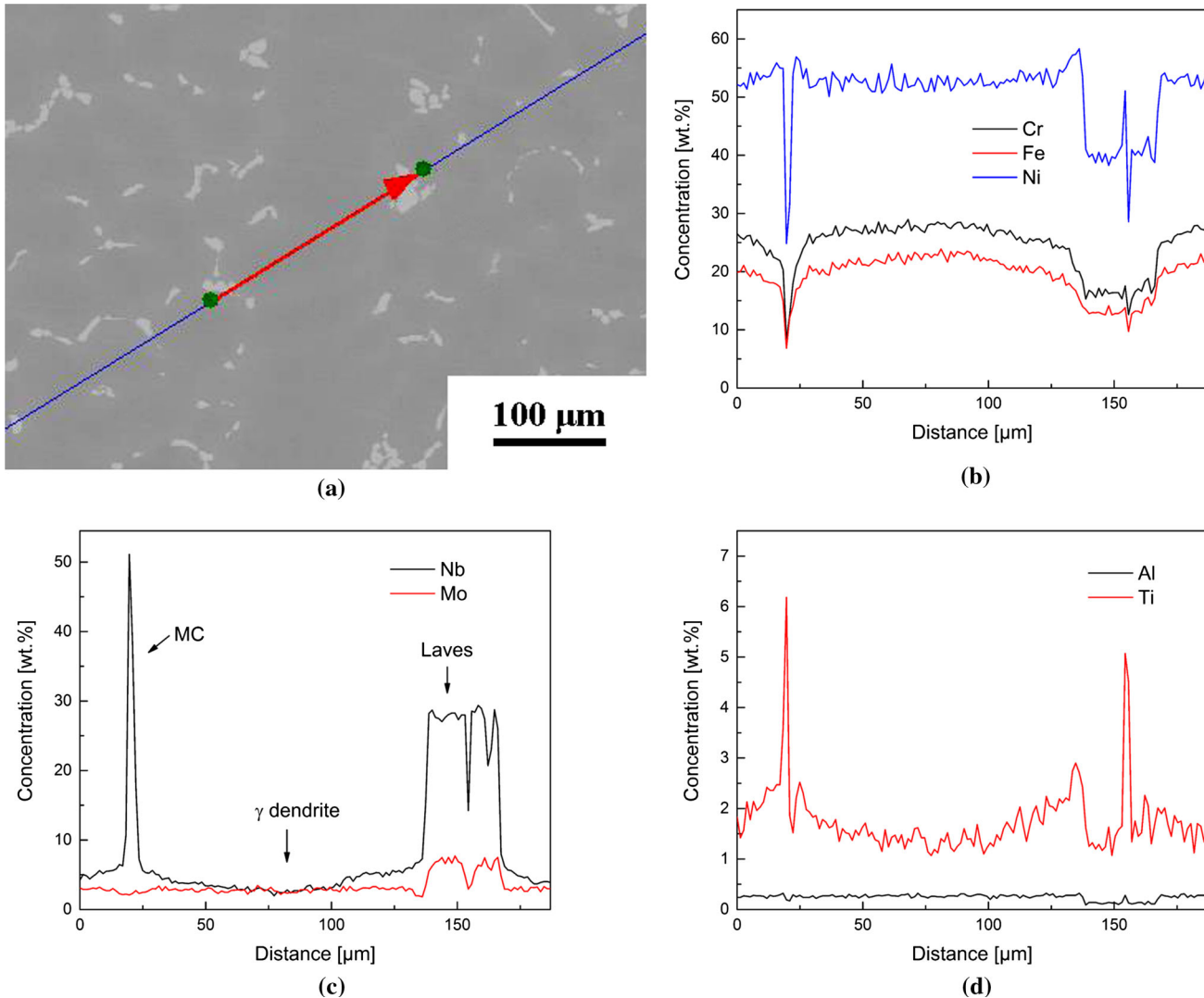

Fig. 10—EPMA profiles obtained across a coarse dendrite of the specimen cooled at 20 °C/min: (a) measurement path; (b) Ni, Cr and Fe; (c) Nb and Mo; (d) Al and Ti.
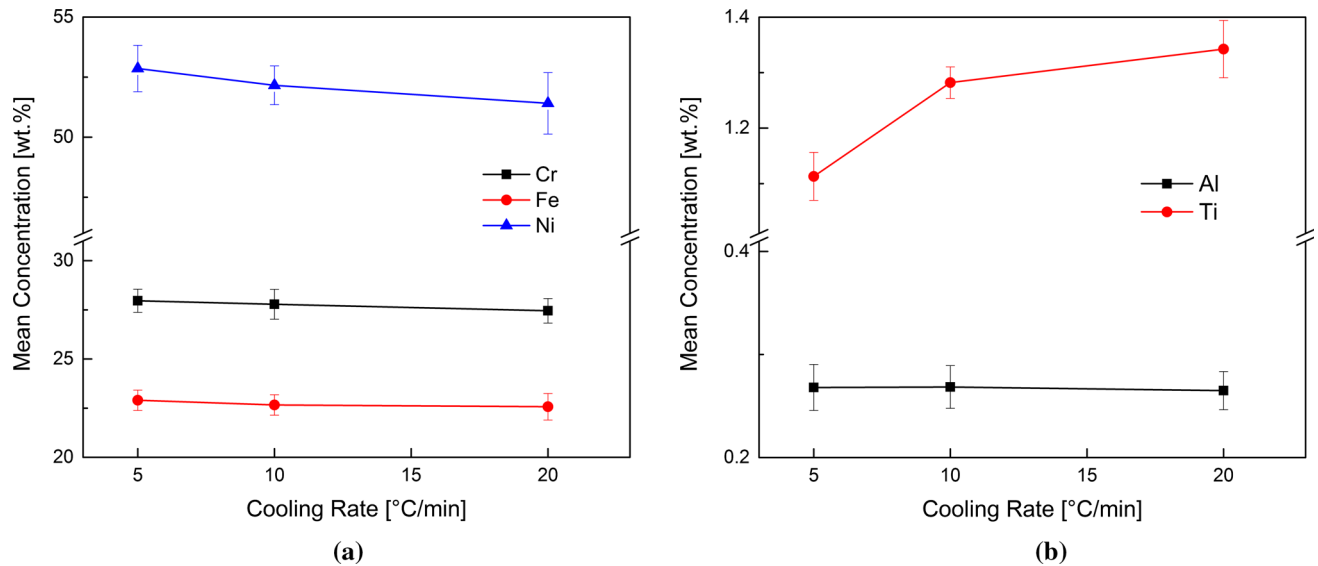
Fig. 11—The correlation between the average element content in dendrite core and the cooling rate: (*a*) Cr, Fe and Ni; (*b*) Al and Ti.

Table IV. Measured Dendrite Core Mean Concentrations and Calculated Effective Partition Coefficients of Nb and Mo in Samples Cooled at Different Rates

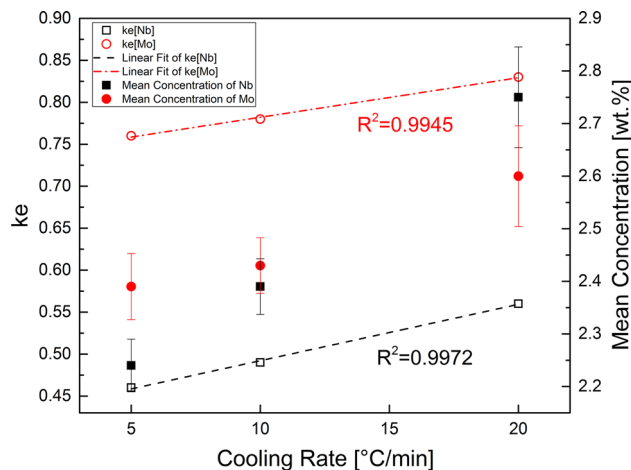| Cooling Rate	5 °C/min	10 °C/min	20 °C/min
Mean concentration of Nb (wt pct)	2.24 ± 0.05	2.39 ± 0.05	2.75 ± 0.09
Mean concentration of Mo (wt pct)	2.39 ± 0.06	2.43 ± 0.05	2.60 ± 0.09
Effective partition coefficients of Nb	0.46	0.49	0.56
Effective partition coefficients of Mo	0.76	0.78	0.83

Fig. 12—Linear fit between the effective partition coefficients and the cooling rates. The Nb and Mo concentrations in dendrite core increase with increasing cooling rate.

at higher cooling rates.[17,20,27] However, the results of the present study demonstrate that the variation of Mo content is still remarkable under slow-cooling conditions; this phenomenon is thus discussed in more detail.

EPMA mapping images of Ni, Nb, Mo, Al, Ti, and C in the interdendritic regions of the samples were recorded to identify the patterns of element segregation and the types of segregated phases. Figure 13 presents

the mapping images of the sample cooled at 5 °C/min, showing that Nb and Mo are enriched in those positions while Ni and Al are depleted. C exhibits a slight dilution in Laves phase but heavily segregates coexisting with Ti and Nb in a few areas, thereby forming MC. The enrichment of Ti at the boundaries of Laves phase is also found. The size and proportion of Laves phase are much larger compared with MC in the cooling conditions studied here.

These results indicate that Nb, Mo, Ti, and C are the principal segregation elements, which are abundant in the segregated phase during solidification and are involved in the reactions promoting the formation of Laves or MC phase. A large amount of large-sized Laves will not only certainly deplete the strengthening elements and reduce the density of hardening precipitates in subsequent thermal processing, resulting in a sharp deterioration of high-temperature performance and low-cycle fatigue life,[5] but also degrade the impact toughness and plasticity because of its low melting point and brittleness. In addition, the fatigue cracking is most likely induced by the MC because of its high thermal stability, which makes coordinate deformation in high-temperature service difficult.[28] Furthermore, because the content of Nb and Mo is much higher than that of Ti and C in IN718 alloy, and because the proportion of MC is much smaller than that of Laves phase, Nb and Mo are considered the major segregative solutes dominating the
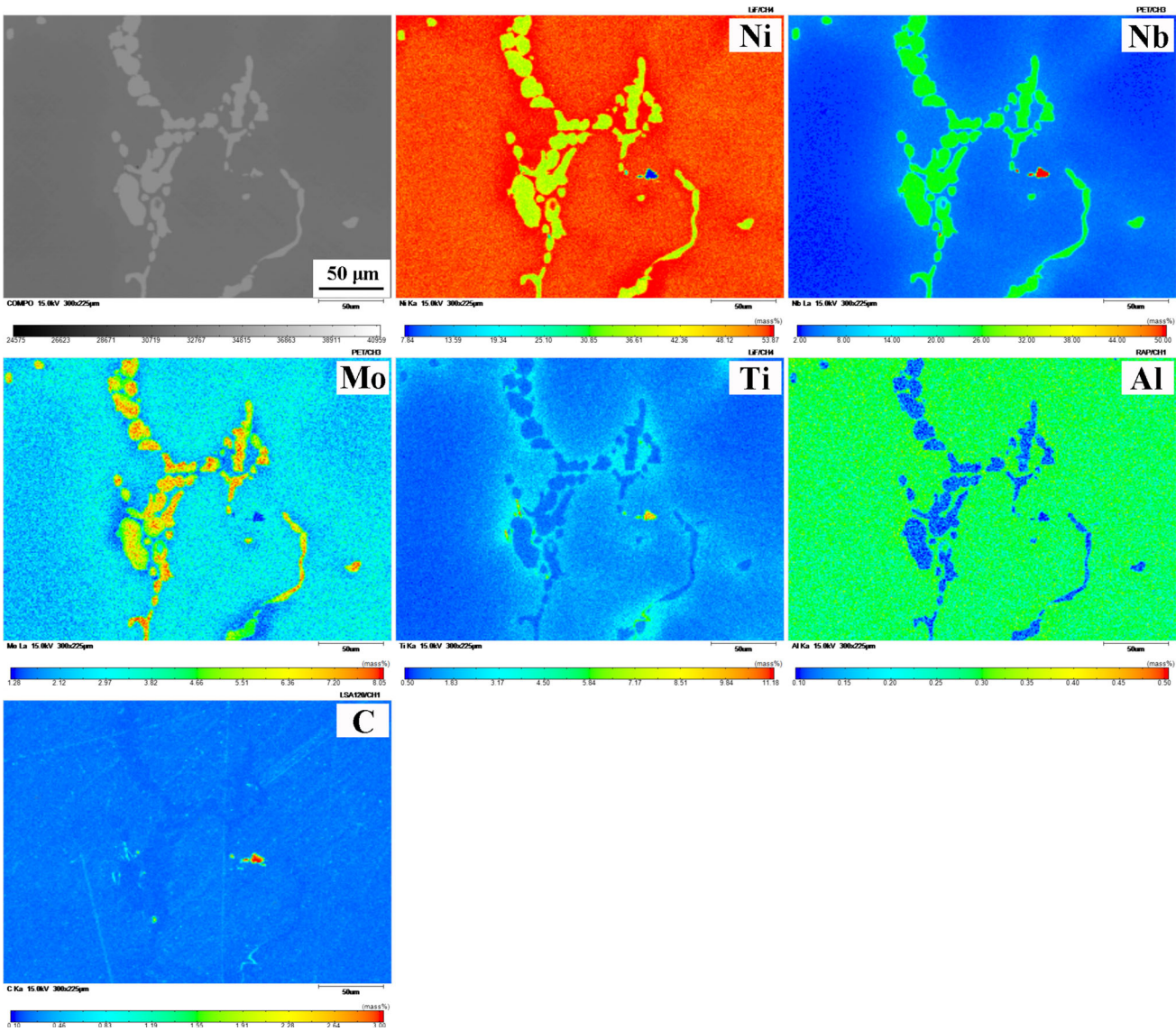
Fig. 13—EPMA mappings of Ni, Nb, Mo, Ti, Al, and C in the specimen cooled at 5 °C/min.

microstructure evolution under slow-cooling conditions.

Normally, the segregation elements will be inevitably enriched in the residual liquid during solidification, and together with the effect of back diffusion, the solute concentrations are constantly changing in both the solid and the liquid phases. Clyne and Kurz[29] have modified the non-equilibrium segregation model developed by Brody and Flemings,[30] who considered the solid-state diffusion in the regime intermediate between the well-known Scheil–Gulliver equation[31] and the lever rule. If it is assumed that the dendrite tips towards a parabolic growth rate, thermodynamic equilibrium is maintained at the liquid-solid interface, and diffusion is infinitely fast in the liquid, the Clyne–Kurz model derives a following expression:

$$C_L = C_0[1 - (1 - 2\Omega(\alpha)k_0)f_S]^{\frac{k_0-1}{1-2\Omega(\alpha)k_0}}, \qquad [3]$$

which may also be written as

$$C_S^* = k_0 C_0[1 - (1 - 2\Omega(\alpha)k_0)f_S]^{\frac{k_0-1}{1-2\Omega(\alpha)k_0}}, \qquad [4]$$

where

$$\Omega(\alpha) = \alpha\left[1 - \exp\left(-\frac{1}{\alpha}\right)\right] - \frac{1}{2}\exp\left(-\frac{1}{2\alpha}\right) \qquad [5]$$

$$\alpha = \frac{D_S t_f}{(0.5\lambda_2)^2}, \qquad [6]$$

where C_0 is the nominal alloy composition; C_S^* is the solid composition near the solid–liquid interface at any solid fraction (f_s); C_L is the liquid composition; D_S is the diffusivity of solute in the solid; t_f is the local solidification time given by the ratio of solidification temperature range to cooling rate; λ_2 is the SDAS, and k_0

Table V. EPMA Quantitative Measurement Results for the Quenched Samples Cooled at 5 °C/min

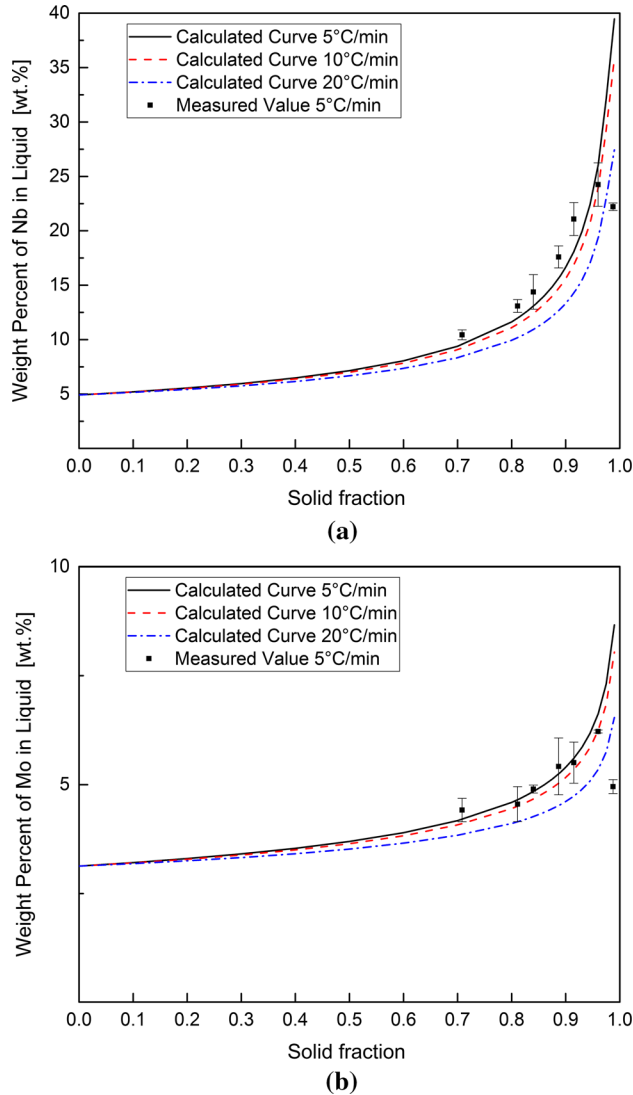| Quench Temperature (°C)	1320	1310	1300	1270	1250	1190	1170
Measured solid fraction	0.71	0.81	0.84	0.89	0.91	0.96	0.99
Average Nb concentration in liquid (wt pct)	10.44 ± 0.45	13.09 ± 0.59	14.39 ± 1.59	17.60 ± 1.01	21.08 ± 1.52	24.25 ± 1.99	22.21 ± 0.35
Average Mo concentration in liquid (wt pct)	4.42 ± 0.27	4.55 ± 0.40	4.90 ± 0.09	5.42 ± 0.65	5.51 ± 0.47	6.22 ± 0.03	4.96 ± 0.16

Fig. 14—The measured results and calculated concentration variations in the liquid: (a) Nb; (b) Mo.

is the equilibrium partition coefficient for the element, which is defined as the ratio of the solid composition to the liquid composition in equilibrium. Assuming that the liquidus and solidus lines of the phase diagram concerned are both straight, then k_0 is a constant.

When solidification is imminent, $f_s \rightarrow 0$; Eq. [4] can then be rewritten as

$$k_0 = C_S^*/C_0. \qquad [7]$$

Provided that the composition of dendrite core is the first solidified component, the k_e could take the place of k_0.

In the previous works,[7,25,32,33] k_0 is invariably used to estimate the concentration profiles in the model, regardless of the solidus deviation at different cooling rates. However, it was confirmed from this study that the effects of constitutional supercooling at the solidification front are different when the cooling rate changes, leading to the difference in deviation degree of the practical solidus. Accordingly, k_e measured in each cooling rate sample is more suitable to its own solidification characterization; hence, it is very meaningful to replace the constant k_0 with the varying k_e to predict the composition change and segregation level under different cooling conditions. Other model parameters used in the simulations for this study are also the results obtained from the current experiments, except for the diffusivities in solids, which were obtained from Reference 34 as 2.3×10^{-14} m²/s for Nb and 9.6×10^{-15} m²/s for Mo.

The calculation curves showing the concentration variation of Nb and Mo in the liquid during the solidification process and the EPMA quantitative measurement results (Table V) of the samples cooled at 5 °C/min and quenched at 1320 °C, 1310 °C, 1300 °C, 1270 °C, 1250 °C, 1190 °C, and 1170 °C are shown in Figure 14. The calculated profile and the experimentally measured data in this figure show excellent agreement, except for the sample quenched at 1170 °C. Combining this information with the DSC results (Figure 1) reveals that the Laves phase starts to form below 1190 °C, leading to a substantial consumption in Nb and Mo content in the residual liquid; therefore, the model is suitable for predicting the liquid composition change before the formation of Laves phase. The calculation results indicate that the concentration of Nb and Mo in the liquid under a lower cooling rate always exceeds those in the liquids under higher cooling rates in the same stage of solidification. Furthermore, the increase in concentration is related to the cooling rate, such that lower cooling rates result in a faster increase of the concentration; thus, the Laves is precipitated earlier. Consistent with the CLSM observations (Figure 2), Table V and Figure 14 show that the solid fraction increases rapidly at the beginning of solidification, with a small amount of liquid always existing, and subsequently does not completely solidify over a wide temperature range. This is the stage in which the liquid concentrations of Nb and Mo increase dramatically, which means that the greater the solid fraction, the faster the concentrations increase.
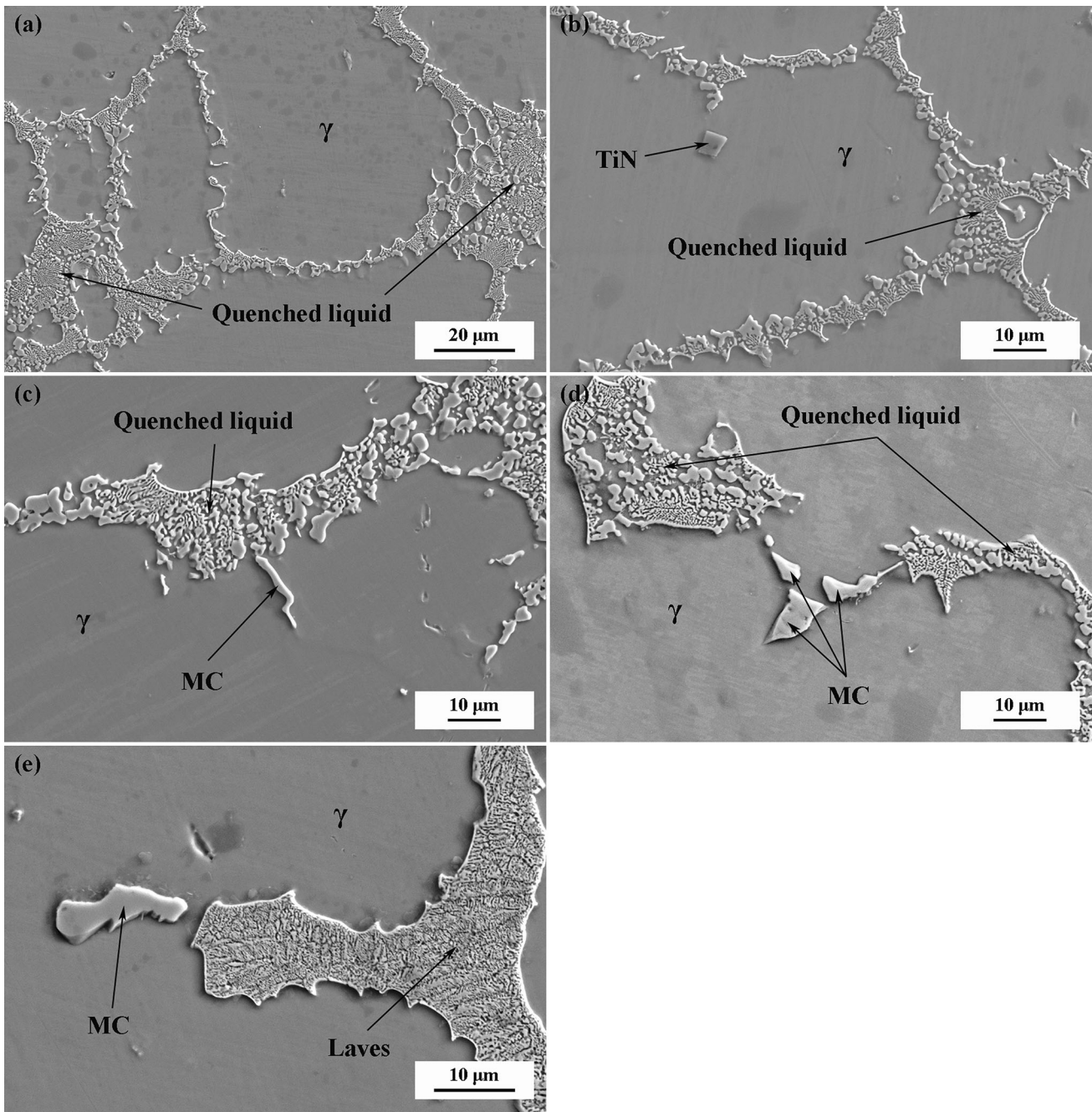
Fig. 15—Solidification microstructures of samples cooled at 5 °C/min and quenched at different temperatures: (*a*) 1320 °C; (*b*) 1300 °C; (*c*) 1250 °C; (*d*) 1190 °C; (*e*) 1170 °C.

Figure 15 presents FESEM images of the solidification microstructures of samples cooled at 5 °C/min and quenched at different temperatures. The area of the quenched liquid decreases with decreasing temperature, and the small cubic TiN is observed inside the γ dendrites at the early stage of solidification. The tiny MC begins to be observed near the remaining liquid in the specimen quenched at 1250 °C. The Laves phase is observed for the first time in the sample quenched at 1170 °C. All of this experimental evidence also validates the modeling results.

The liquid composition variation, elemental distribution, microstructural evolution, and morphology change of the solid–liquid interface at different cooling rates during solidification can well reflect the degree of segregation. The findings in the current work are expected to conduct fundamental research on microsegregation behaviors of as-cast IN718 alloy and offer basic experimental data in slow-cooled conditions. The characteristics and laws investigated and analyzed in this work could correspond to industrial samples to reveal common features and provide reference data.

IV. CONCLUSIONS

A detailed microsegregation analysis of as-cast IN718 alloy samples cooled at various slow rates has been performed. The following conclusions were drawn from the present study.

1. The morphology of the solid-liquid interface is greatly influenced by the cooling rate. The γ cell crystals on the interface grow into regular hexagonal structures and the intercellular regions become a continuous reticulation when the cooling rate is 5 °C/min. As the cooling rate increases, the cellular interface becomes irregular.

2. The volume fraction of the segregated phase in samples cooled at 5, 10, and 20 °C/min is 3.70, 2.92, and 2.36 vol pct, respectively, showing a continuous decrease with increasing cooling rate. A much larger amount of the Laves phase is precipitated than the MC during solidification; however, the Laves phase shows no apparent variation in composition within the range of slow-cooling rates investigated in this study. The prediction formula of SDAS for IN718 under slow-cooled conditions is established as $\lambda_2 = 258(GR)^{-1/3}$.

3. The contents of Ni, Cr, Fe, and Al tend to slightly decrease with increasing cooling rate, whereas the contents of Nb, Mo, and Ti tend to increase in the dendrite core. Mo is found to be one of the major segregation solutes, similar to Nb, dominating the microsegregation under slow-cooling conditions. The effective partition coefficients of Nb and Mo exhibit an almost linear increase with increasing cooling rate. The measured k_e[Nb] under cooling rates of 5, 10, and 20 °C/min are 0.46, 0.49, and 0.56, respectively; the corresponding k_e[Mo] values are 0.76, 0.78, and 0.83, respectively.

4. The variation trends of the Nb and Mo concentrations in the liquid during solidification at different cooling rates were achieved by calculation using the Clyne–Kurz equation in combination with the present experimental parameters. Reasonable agreement was obtained between the calculated curves and measured values before the formation of Laves phase. The results indicate that the greater the solid fraction or the lower the cooling rate, the faster the concentrations of Nb and Mo in the liquid metal increase.

REFERENCES

1. Q.Z. Zuo, F. Liu, L. Wang, and C. Chen: *Metall. Mater. Trans. A*, 2013, vol. 44A, pp. 3014–27.
2. D.H. Ping, Y.F. Gu, C.Y. Cui, and H. Harada: *Mater. Sci. Eng. A*, 2007, vol. 456, pp. 99–102.
3. D.K. Oh, C.Y. Jo, H.C. Kim, J.H. Lee, and S.L. Lee: *Met. Mater. Int.*, 2000, vol. 6, pp. 311–15.
4. A. Thomas, M. El-Wahabi, J.M. Cabrera, and J.M. Prado: *J. Mater. Process. Tech.*, 2006, vol. 177, pp. 469–72.
5. Y.C. Liu, Q.Y. Guo, C. Li, Y.P. Mei, X.S. Zhou, Y. Huang, and H.J. Li: *Acta Metall. Sin.*, 2016, vol. 52, pp. 1259–66.
6. J.N. DuPont, C.V. Robino, J.R. Michael, M.R. Notis, and A.R. Marder: *Metall. Mater. Trans. A*, 1998, vol. 29A, pp. 2785–96.
7. G.A. Knorovsky, M.J. Cieslak, T.J. Headley, A.D. Romig, Jr, and W.F. Hammetter: *Metall. Trans. A*, 1989, vol. 20A, pp. 2149–58.
8. W.D. Cao: *Superalloys 718, 625 and Various Derivatives*, TMS, Warrendale, PA, 1991.
9. S.G.K. Manikandan, D. Sivakumar, K. Prasad Rao, and M.J. Kamaraj: *Mater. Process. Tech*, 2014, vol. 214, pp. 3141–49.
10. A.G. Kostryzhev, P. Mannan, and O.O. Marenych: *J. Mater. Sci.*, 2015, vol. 50, pp. 7115–25.
11. N.B. Dahotre, M.H. McCay, T.D. McCay, C.R. Hubbard, W.D. Porter, and O.B. Cavin: *Scr. Metall. Mater.*, 1993, vol. 28, pp. 1359–64.
12. T.J. Watt, E.M. Taleff, L.F. Lopez, J. Beaman, and R. Williamson: *Solidification Mapping of a Nickel Alloy 718 Laboratory VAR Ingot*, TMS, San Antonio, TX, 2013.
13. J.J. Blecher, T.A. Palmer, and T. Debroy: *Metall. Mater. Trans. A*, 2014, vol. 45A, pp. 2142–51.
14. W. Yang, K.M. Chang, W. Chen, S. Mannan, and J. Debarbadillo: *Metall. Mater. Trans. A*, 2001, vol. 32A, pp. 397–406.
15. C. Frueh, D.R. Poirier, R.G. Erdmann, and S.D. Felicelli: *Mater. Sci. Eng. A*, 2003, vol. 345, pp. 72–80.
16. Z.D. Long, X.B. Liu, W.H. Yang, K.M. Chang, and E. Barbero: *Mater. Sci. Eng. A*, 2004, vol. 386, pp. 254–261.
17. S.G.K. Manikandan, D. Sivakumar, K. Prasad Rao, and M. Kamaraj: *Mater. Charac*, 2015, vol. 100, pp. 192–206.
18. L. Wang, Y.J. Yao, J.X. Dong, and M.C. Zhang: *Chem. Eng. Commun.*, 2010, vol. 197, pp. 1571–85.
19. T. Antonsson and H. Fredriksson: *Metall. Mater. Trans. B*, 2005, vol. 36B, pp. 85–96.
20. S.G.K. Manikandan, D. Sivakumar, K.P. Rao, and M. Kamaraj: *J. Mater. Process. Tech.*, 2014, vol. 214, pp. 358–64.
21. Y.N. Yu: *Foundation of Materials Science*, China Higher Education Press, Beijing, 2006, pp. 636–80.
22. J. Li, L.X. Yu, W.R. Sun, W.H. Zhang, F. Liu, F. Qi, S.R. Guo, and Z.L. Hu: *Chin. J. Mater. Res.*, 2010, vol. 2, pp. 118–22.
23. Z.J. Miao, A.D. Shan, W. Wang, J. Lu, W.L. Xu, and H.W. Song: *Trans. Nonferrous Met. Soc. China*, 2011, vol. 21, pp. 236–42.
24. H. Shibata, H. Yin, S. Yoshinaga, T. Emi, and M. Suzuki: *ISIJ Int.*, 1998, vol. 38, pp. 149–56.
25. J.N. DuPont: *Metall. Mater. Trans. A*, 1996, vol. 27A, pp. 3612–20.
26. W. Kurz and D.J. Fisher: *Acta Metall.*, 1981, vol. 29, pp. 11–20.
27. M.J. Perricone and J.N. DuPont: *Metall. Mater. Trans. A*, 2006, vol. 37A, pp. 1267–80.
28. S. Biswas, G.M. Reddy, T. Mohandas, and C.V.S Murthy: *J. Mater. Sci*, 2004, vol. 39, pp. 6813–15.
29. T.W. Clyne and W. Kurz: *Metall. Trans. A*, 1981, vol. 12A, pp. 965–71.
30. T.F. Bower, H.D. Brody, and M.C. Flemings: *Trans. TMS-AIME*, 1966, vol. 236, pp. 624–33.
31. E. Scheil: *Z. Metallkd.*, 1942, vol. 34, pp. 70–72.
32. M.J. Cieslak, T.J. Headley, G.A. Knorovsky, A.D. Romig, Jr, and T. Kollie: *Metall. Mater. Trans. A*, 1990, vol. 21A, pp. 479–88.
33. L. Nastac: *Metall. Mater. Trans. B*, 2014, vol. 45B, pp. 44–50.
34. Y.A. Meng and B.G. Thomas: *Metall. Mater. Trans. B*, 2003, vol. 34B, pp. 685–705.